

pubs.acs.org/acscatalysis Research Article

Two-Dimensional Palladium Nanosheet Intercalated with Gold Nanoparticles for Plasmon-Enhanced Electrocatalysis

Jianwei Ding, Fengmei Wang, Feng Pan, Peng Yu, Ning Gao, Randall H. Goldsmith, Shuangfei Cai, Rong Yang, and Jun He*



Cite This: ACS Catal. 2021, 11, 13721-13732



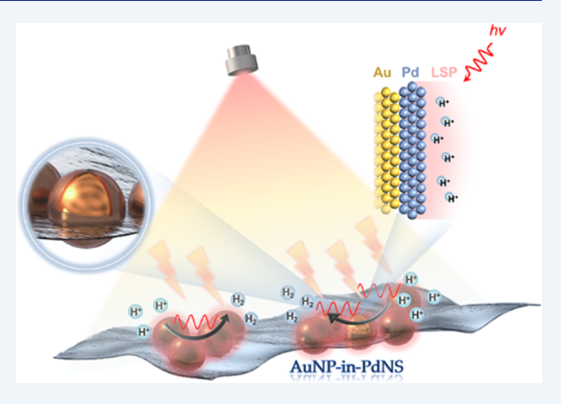
ACCESS

Metrics & More



Supporting Information

ABSTRACT: Plasmon-enhanced electrocatalysis holds great promise for converting solar energy into chemical energy by efficiently harvesting photons for electrocatalytic reactions. Here, we report a unique two-dimensional (2D) "Egg Waffle"-like heterostructure, i.e., gold nanoparticles intercalated in a palladium nanosheet (AuNP-in-PdNS), effectively interfacing Au NPs with 2D Pd for greatly enhancing electrocatalytic activity under light illumination. A considerable electrocatalytic enhancement, i.e., a small overpotential of 19 mV (i.e., 4-fold decrease) at a current density of 10 mA cm⁻² for the hydrogen evolution reaction and an improved oxygen reduction reaction with a half-wave potential of 0.882 V, is achieved on the 2D AuNP-in-PdNS heterostructure due to excitation of the localized surface plasmon resonance (LSPR). The unique heterostructure and strongly enhanced localized field intensity under LSPR excitation could result in hot electrons concentrated on



the surface of Pd NSs and direct transfer of plasmonic energy to metal—adsorbate complexes, manifesting as a reduction of the apparent activation barrier in the electrocatalysis. This study provides insight into both the design of efficient electrocatalysts and the distinct role of LSPR excitation in plasmon-enhanced electrocatalysis.

KEYWORDS: 2D heterostructure, electrocatalysis, plasmon effect, palladium nanosheet, gold nanoparticle

1. INTRODUCTION

Plasmon-enhanced catalysis has recently emerged as a thrilling field where solar energy is efficiently harvested to drive chemical transformations for energy conversion. 1-3 The excitation of collective oscillations of free conduction electrons, also known as localized surface plasmon resonances (LSPRs), results from strong visible light-matter interactions in plasmonic nanomaterials (Au, Ag, or Cu). These LSPRs give rise to strongly enhanced light absorption and localized electromagnetic field intensity, facilitating energy and electron transfer during reactions. Nevertheless, these plasmonic nanomaterials alone catalyze only limited types of reactions under light illumination. A variety of bimetallic nanostructures that combine plasmonic metals and catalytic metals (palladium, platinum, rhodium, etc.), such as the antenna-reactor, core—shell structure, and alloys, she have been reported and exhibited excellent performance in catalysis. The created electromagnetic hotspots underpin improved chemical kinetics and reaction rates seen in different catalytic reactions.6,18-22

In particular, plasmon-enhanced electrocatalysis, in which the excitation of LSPRs is coupled with an applied potential to improve catalysts' selectivity and activity, offers an opportunity to lower the activation barrier for chemical conversions and constitutes a critical strategy for sustainable production of fuels or value-added chemicals. Some typical electrochemical reactions, such as carbon dioxide reduction, ²³ oxygen reduction, ^{24,25} and hydrogen evolution reactions, ^{26,27} are promoted by the plasmons. Unfortunately, the inherent chemical inertness of common plasmonic noble metals (e.g., Au or Ag)²⁸ constrains their wide applications in electrocatalysis. To remedy this situation, various supported structures combining plasmonic nanostructured metals with efficient electrocatalysts have been established. 24,25,29,30 Indeed, important and often surprising structure-function relationships in recent studies have begun to imply that the two-dimensional (2D) nature of the electrocatalyst is important.^{24,30,31} Ultrathin 2D nanostructures are attractive to mingle with plasmonic metals for providing a versatile and effective platform for electrocatalysis with abundant active sites to adsorb species, high specific surface area, and fast electron transport. But, the most commonly reported structures are plasmonic nanostructures decorated on the surface of the 2D

Received: August 23, 2021 Revised: October 16, 2021 Published: October 28, 2021





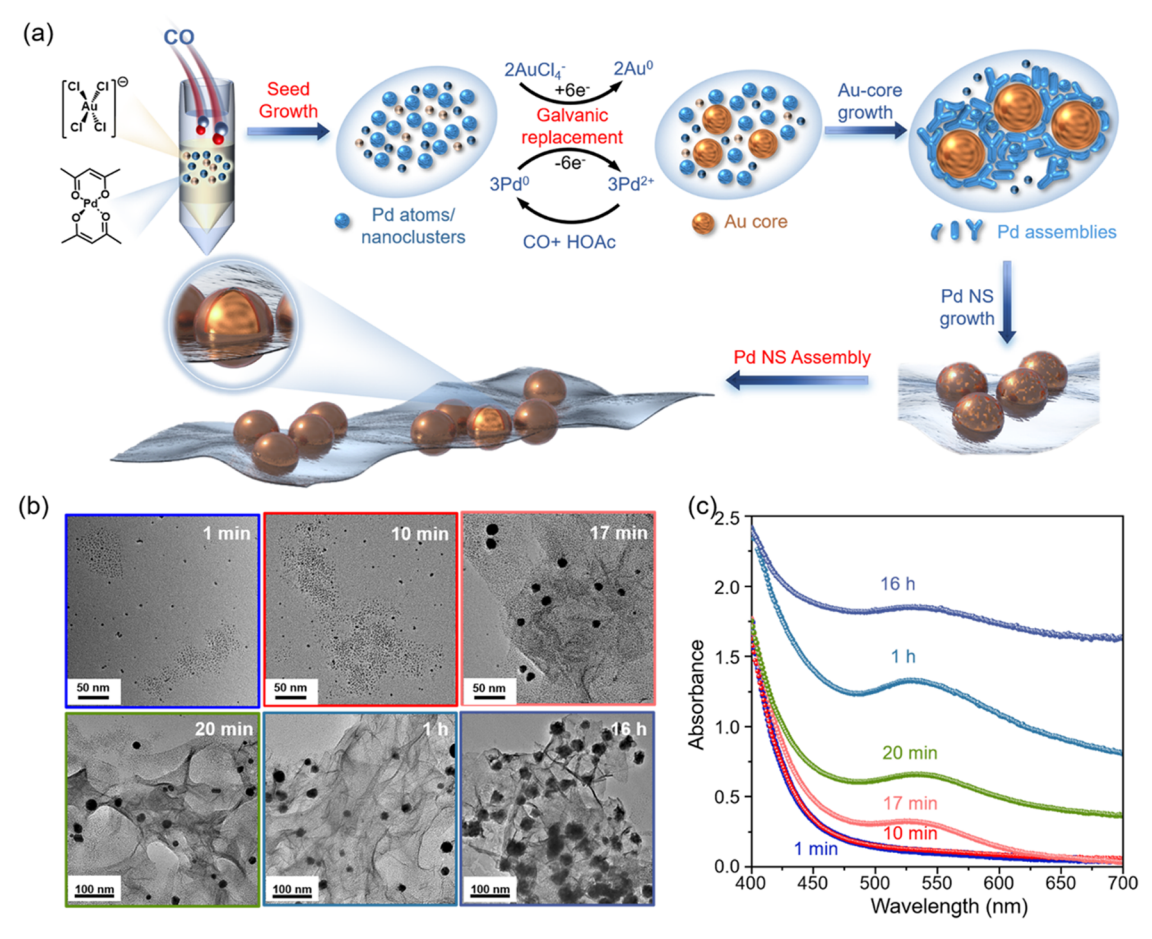


Figure 1. Synthesis of the 2D AuNP-in-PdNS heterostructure. (a) Schematic illustration for the formation process, including seed growth, galvanic replacement, and assembly steps, of the 2D AuNP-in-PdNS heterostructure. (b) Ex situ TEM characterization of the intermediates extracted at different reaction times (1, 10, 17, 20, 60 min, and 16 h) during the synthesis process, clearly showing the formation of the 2D Au_{0.15}NP-in-PdNS heterostructure. (c) Corresponding UV—Vis absorption spectra of the intermediate solutions shown in (b).

electrocatalysts.^{24,30} On the one hand, these heterostructures potentially limit the contact between the reactants and the catalytically active sites, preventing catalytic performance from further being improved. On the other hand, a strongly enhanced electromagnetic field may not be fully utilized because the field polarized in certain directions favorably enhances charge excitations and concentrates hot carriers in the areas away from some catalytically active sites. Thus, a powerful new strategy for maximizing electrocatalytic activity would be to interface plasmonic nanoparticles with 2D electrocatalysts.

Here, we report a novel 2D heterostructure with gold nanoparticles intercalated in a palladium nanosheet (AuNP-in-PdNS) to enhance electrocatalytic activity under the LSPR excitation. A facile wet-chemical method that combines seed growth, galvanic replacement, and assembly in one step (denoted as the SGA method) was developed to synthesize the 2D AuNP-in-PdNS heterostructure (Figure 1a), which demonstrates an "Egg Waffle"-like structure. This heterostructure, which features ultrathin (~1.4 nm) Pd NS wrapping Au NPs, integrates all of the advantages of 2D nanostructures with the plasmonic effect offered by Au NPs for boosting electrocatalysis. Specifically, we investigated its electrocatalytic activity in the hydrogen evolution reaction (HER) and the oxygen reduction reaction (ORR) under light illumination, showing strongly enhanced reduction of H⁺ to H₂ and O₂

reduction by leveraging the simultaneous LSPR excitation of Au NPs intercalated in Pd NS. Conspicuously lowered overpotential, increased limiting current density, accelerated kinetics, and wavelength-dependent catalytic enhancement are observed. Our electromagnetic simulations shed light upon the underlying mechanism of plasmonic enhancement, underscoring the importance of plasmon-enhanced absorption and unique plasmonic modal properties in the AuNP-in-PdNS along with favorable interband transitions in Pd NS. These attributes significantly contribute to efficient hot-carrier generation in the Pd NS that wraps the Au NP and possibly mediate a direct transfer of plasmonic energy to the metaladsorbate complex while activating a new desorption pathway in the HER, both of which synergistically enable the apparent activation barrier to substantially decrease from 9.43 to 7.29 kJ mol^{-1} .

2. RESULTS AND DISCUSSION

2.1. Synthetic Method and Formation Mechanism of the 2D AuNP-in-PdNS Heterostructure. To date, some 2D nanostructures based on Au or Pd NSs have been created by means of several synthetic strategies, including seeded growth, organic ligand-assisted growth, and crystal phase transformation. Typically, multiple steps of prepreparation, surface modification of supports, and in situ growth/immobilization of metals are involved in these conventional

protocols. Here, we developed a spontaneously combined seed growth-galvanic-replacement-assembly (named as SGA) method for constructing the AuNP-in-PdNS heterostructure. All reactants, including metal precursors (Pd(acac), and $HAuCl_{\lambda} \cdot xH_{2}O$) and solvent (acetic acid), were simultaneously added into a reactor vessel, followed by bubbling CO gas to initiate synthesis. The reaction was conducted at room temperature under surfactant-free conditions without any reductant or stabilizer (see Section 4 for detailed information). An intriguing feature lies in the fact that the Au NPs are not coated on the surface of the Pd NS but buried within the body of the Pd NS (detailed structural characterization is shown later). As illustrated in Figure 1a, the Pd⁰ atoms/nanoclusters acting as seeds were first formed when introducing CO gas through the coordination reaction, after which the subsequent galvanic replacement between Pd⁰ and Au³⁺ was spontaneously driven to obtain Au NPs due to the more positive reduction potential (1.50 V) of Au³⁺/Au⁰ than that of Pd²⁺/Pd⁰ (0.915 V).35 The simultaneous galvanic replacement and assembly processes finally gave rise to the formation of the 2D AuNP-in-PdNS heterostructure. In comparison, there was no product observed if only HAuCl₄·xH₂O was added, whereas the Pd NSs could be formed if only Pd(acac), was introduced during synthesis (see the Supporting Information for detailed information, Figure S1), concluding the necessity of the specific coordination reaction among Pd(acac)2, acetic acid, and CO for building the 2D architecture. 36,37 The control studies on other reaction conditions, including the choice of metal precursors (see the Supporting Information for detailed information, Figure S2a,b), the usage of CO or acetic acid (see the Supporting Information for detailed information, Figure S2c,d), and participation of water (see the Supporting Information for detailed information, Figure S2e,f), also further verify this finding. Meanwhile, employing both precursors with various ratios of Au^{3+} to Pd^{2+} (denoted as x) produces similar 2D heterostructures. By tuning x (i.e., 0.05, 0.10, 0.15, 0.20, 0.50, 1.0, and 2.0), a series of 2D heterostructured samples (denoted as Au, NP-in-PdNS) with a similar lateral size (around 2 μ m) were obtained. From scanning electron microscopy (SEM, Figure S3) and transmission electron microscopy (TEM, Figure S4) images, the size of Au NPs increases from 13.6 to 45.7 nm when α increases from 0.05 to 0.50, but there is no significant change in the thickness (\sim 1.4 nm) of the Pd NS (Figure S5). If x >1.0, no intact Pd NS but a conspicuous aggregation of Au NPs is observed (Figure S4f,g). The composition obtained from inductively coupled plasma optical emission spectrometry (ICP-OES) was very close to the theoretical ratios of Au to Pd after the galvanic-replacement step (Table S1). To further unravel the reaction mechanism, taking the synthesis of Au_{0.15}NP-in-PdNS as an example, the reaction was monitored by characterizing a series of aliquots of the reaction solution via both ex situ TEM and UV-Vis absorption spectroscopy at specific reaction time points (see the Supporting Information for detailed information, Figures S6 and S7). Figure 1b presents the corresponding TEM images, including the generation of Pd atoms/nanoclusters as seeds (i.e., seed growth), replacement of Pd seeds for producing Au NPs (i.e., galvanic replacement), and the Pd NS formed surrounding the Au NP (i.e., assembly). The gradually growing absorption peak at ~530 nm and its slight redshift observed in UV-Vis spectra (Figures 1c and S7a) within 20 min in the reaction indicates the formation of the Au NP; while after 20 min, the overall

ascending absorption envelope suggests the formation of the Pd NS around the Au NP (Figure S7b). Based on these characterization methods, the formation mechanism is proposed as follows: (i) first, the preferential coordination reaction of three reactants (Pd²⁺ ions, CO, and acetic acid) rapidly gave rise to Pd atoms/nanoclusters as seeds/nucleation sites (within 1 min), enabling subsequent galvanic replacement between the Pd atoms and Au³⁺ ions for Au NP production; (ii) then, the size of Au NP kept increasing, which is suggested by gradually growing and slightly redshift LSPR absorption feature at ~530 nm within 20 min (Figures 1c and S7a), until all of the Au³⁺ ions were consumed with repeated reduction of Pd²⁺ ions and replacement; (iii) Pd atoms/nanoclusters were continuously generated around the Au NP, and finally assembled into the Pd NS (Figure S8) along the [111] direction with the help of the CO confinement effect,³⁸ which is indicated by increasing absorbance in the whole absorption envelope seen in the formation process of the heterostructures (Figures 1c and S7b).

Figure 2a displays a TEM image of the as-obtained 2D Au_{0.15}NP-in-PdNS heterostructure, demonstrating lots of

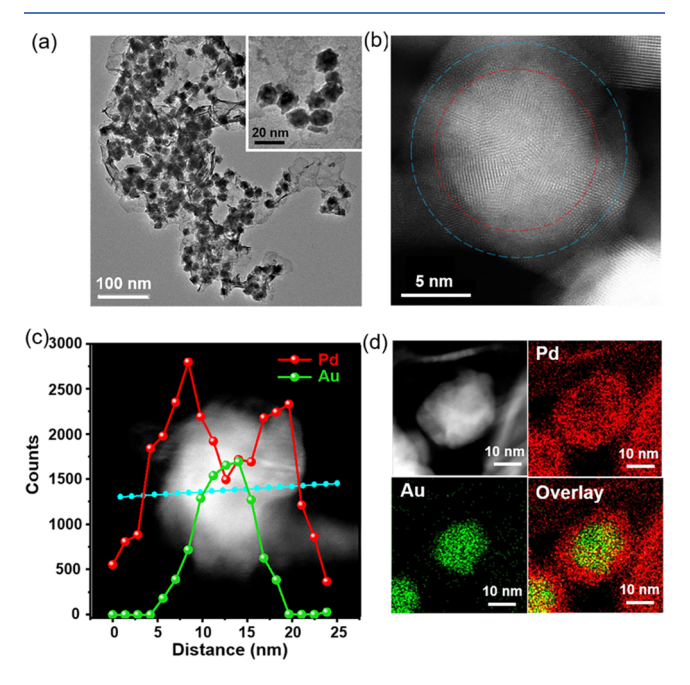


Figure 2. Structural characterization of the 2D $Au_{0.15}NP$ -in-PdNS heterostructure. (a) TEM images under different magnifications. (b) HAADF-STEM image collected around one Au NP. The red and blue circles represent the Au–Pd interface and the Pd NS shell, respectively. (c) EDX line-scanning profile across a single Au NP intercalated in the Pd NS, clearly showing that Au atoms dominate in the middle and Pd atoms are around the Au core. (d) Corresponding EDX mapping images of Pd and Au elements further confirm that the Au NP intercalated in the Pd NS.

spherical NPs (about 15 nm in diameter) intercalated in the body of ultrathin Pd NSs with an interesting Egg Waffle-like morphology. To acquire more detailed structural information, high-angle annular dark-field scanning transmission electron microscopy (HAADF-STEM) was employed. As shown in Figure 2b, the Au NP core (marked in red line) is buried in the ultrathin Pd NS shell (marked in blue line). A clear lattice spacing of 0.225 nm observed upon and around the Au NP core suggests that the Pd NS with the (111)-facet is formed

ACS Catalysis pubs.acs.org/acscatalysis Research Article

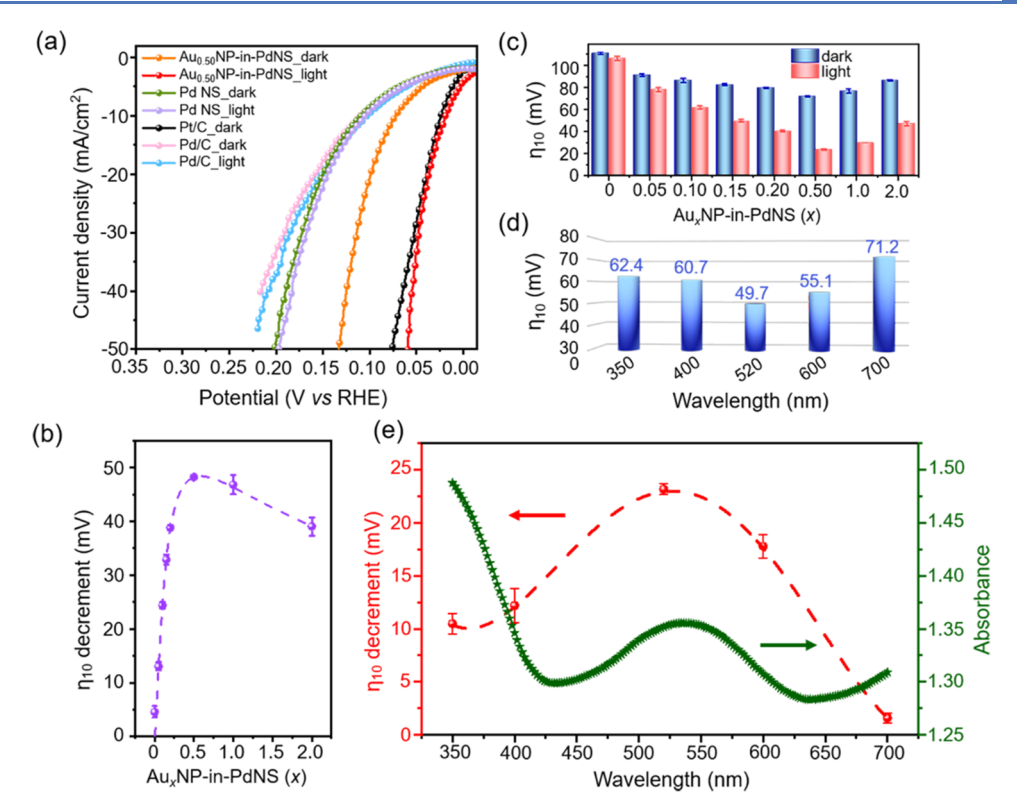


Figure 3. Plasmon-enhanced hydrogen evolution reaction electrocatalysis on the 2D AuNP-in-PdNS heterostructure at room temperature. (a) Polarization curves collected on the $Au_{0.50}NP$ -in-PdNS electrode at a scan rate of 10 mV s⁻¹ under Xenon light illumination (200 mW cm⁻²) and dark conditions. In comparison, the commercial 20 wt % Pt/C and Pd/C were also tested under the same conditions. (b) $η_{10}$ decrement, i.e., the difference in the overpotential at 10 mA cm⁻² between dark and Xenon light illumination conditions, for various Au_xNP -in-PdNS electrodes. (c) $η_{10}$ values collected from various Au_xNP -in-PdNS electrodes under dark (blue) and light illumination (red) conditions. (d) Wavelength-dependent $η_{10}$ values collected from the $Au_{0.50}NP$ -in-PdNS electrode, showing the smallest $η_{10}$ at 520 nm. (e) Wavelength-dependent $η_{10}$ decrement (red) before and after light illumination obtained on the $Au_{0.50}NP$ -in-PdNS electrode, along with a UV–Vis absorption spectrum of the catalyst (dark green). Data are presented as the mean of three independent experiments, and error bars signify standard errors. The same light intensity of 16.8 mW cm⁻² was utilized for the measurements in (d) and (e).

(Figure S8). Meanwhile, both the line-scan profile across a single Au NP by energy-dispersive X-ray spectroscopy (EDX) (Figure 2c) and EDX mapping images at different magnifications (Figures 2d and S9) show that Au NPs are intercalated within the body of the Pd NS, further confirming the formation of the 2D AuNP-in-PdNS heterostructure. The X-ray diffraction (XRD) and X-ray photoelectron spectroscopy (Figures S10 and S11) verify the coexistence of separate Au and Pd phases instead of the alloyed Au—Pd nanostructure.

2.2. Plasmon-Enhanced Hydrogen Evolution and Oxygen Reduction on the Au_xNP-in-PdNS. Given Pd NS's two-dimensional (2D) nature that provides a large catalytic surface area and plasmon-driven processes induced by optical plasmon-excitation of Au NPs in the 2D AuNP-in-PdNS heterostructure, we investigated the electrocatalytic activity of the Au, NP-in-PdNS under light illumination. First, the hydrogen evolution reaction (HER) is focused here due to its promising activity in palladium-based materials and a oneelectron process during the electrochemical reaction.³⁹ The electrochemical measurements were conducted in a typical three-electrode system in acidic $HClO_4$ solution (1 M, pH \approx 0.09), where the Au_xNP-in-PdNS (x = 0.05, 0.10, 0.15, 0.20,0.50, 1.0, and 2.0) catalyst was drop-casted on a rotating disk electrode (RDE) acting as the working electrode (see Section 4 for detailed information) and a Xenon light lamp was utilized as a light source to irradiate the working electrode surface (Figures S12 and S13). In comparison, the commercial Pt/C

and Pd/C catalysts were also tested under the same conditions. Polarization curves (Figures 3a and S14) show a superior HER performance with an overpotential of 19.0 mV at a current density of 10 mA cm⁻² (i.e., η_{10}) for the Au_{0.50}NP-in-PdNS catalyst under light illumination. It is noted that the geometric surface area (0.196 cm²) of RDE is used to normalize current densities in all electrochemical measurements if they are not specified. Even the electrochemical surface area (ECSA) of the various electrocatalysts is used to normalize the current density, and the Au_{0.50}NP-in-PdNS still demonstrates the best performance (Figure S16). Compared to the control experiment under dark conditions (72.4 mV of η_{10}), a 4-fold decrease is achieved. In other words, an overpotential decrement (i.e., the difference of η_{10} between the dark and light illumination conditions) of 53.4 mV is obtained, suggesting a considerable enhancement in hydrogen evolution. Notably, the catalytic activity of the Au_{0.50}NP-in-PdNS under light illumination outperforms the benchmark of Pt/C (Figure 3a) and other reported catalysts (Table S3) in acidic media. The smaller overpotential for the HER on the Pd NS, compared with other structures (Table S2), also indicates the improved activity of the two-dimensional structure. A much lower Tafel slope of 37 mV dec⁻¹ and a smaller charge-transfer resistance (R_{ct} , 21.7 Ω) (Figures S15 and S17 and Table S6) are found in the $Au_{0.50}NP$ -in-PdNS catalyst under light illumination than those (79 mV dec $^{-1}$ and 108.9 Ω) under dark conditions, revealing improved kinetics of the HER. ACS Catalysis pubs.acs.org/acscatalysis Research Article

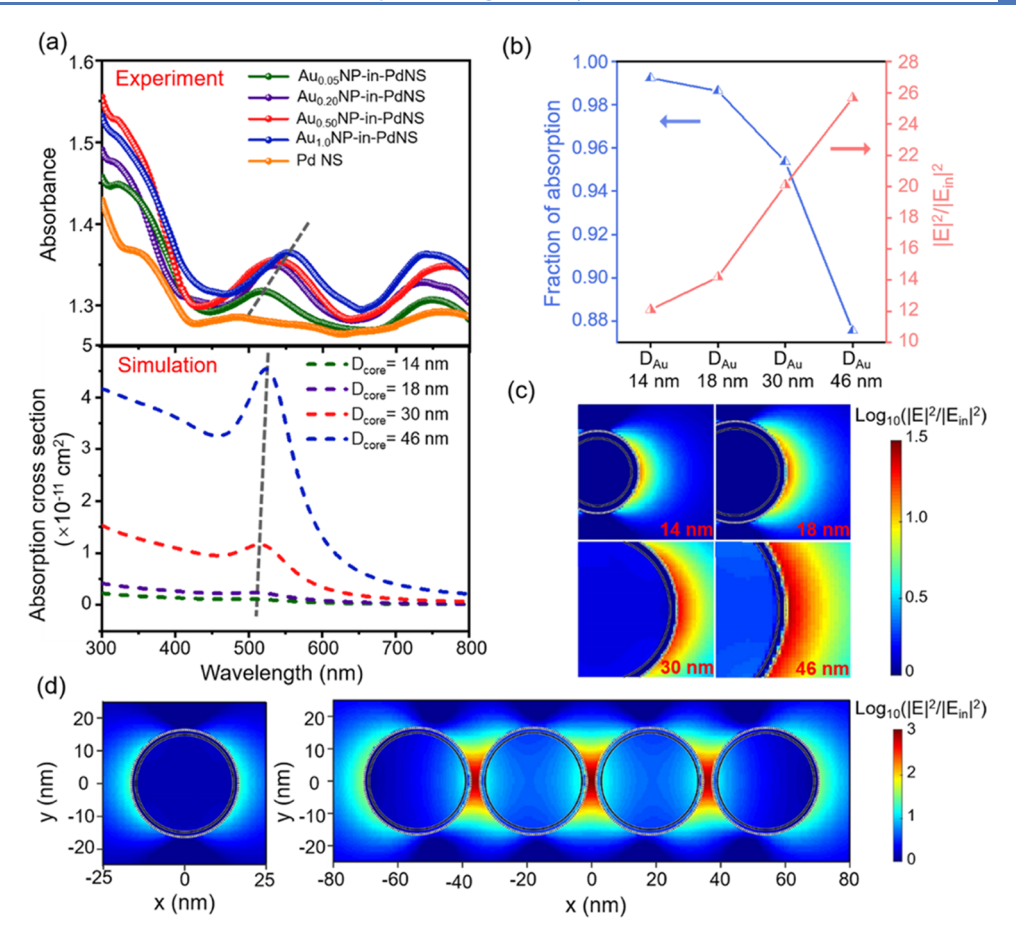


Figure 4. Electromagnetic simulations for the Au_xNP-in-PdNS heterostructure. (a) Experimental absorption spectra (top) for a series of the Au_xNP-in-PdNS heterostructures combined with the pure Pd NS and simulated absorption spectra (bottom) for the corresponding Au_xNP-in-PdNS core—shell nanostructures. (b) Calculated fraction of absorption and maximum field enhancement factors for the Au_xNP-in-PdNS core—shell nanostructures at a wavelength of 548 nm. (c) Two-dimensional field enhancement profiles for the Au_xNP-in-PdNS core—shell nanostructures, where the interface between the Au core and the Pd shell is marked by a black circle and the outer surface of the Pd shell marked by a white dashed line. (d) Comparison of field enhancement profiles between single and aggregated Au_{0.50}NP-in-PdNS nanostructures.

Clearly, the obvious decrease in the Tafel slope from 79 to 37 mV dec⁻¹, which is very close to the value (34 mV dec⁻¹) in the Pt/C catalyst, suggests that the Volmer-Tafel mechanism dominates under light illumination with Tafel desorption as the limiting step. The continuous chronopotentiometry test (Figure S18) by alternating dark and light illumination signifies an additional photopotential (or photocharging) experienced by the electrode, ²⁷ resulting in the accelerated rate of electron transfer from the Au_{0.50}NP-in-PdNS electrocatalyst to protons in solution. This result is consistent with the reduced chargetransfer resistance and lowered overpotential. A much higher H_2 gas evolution rate (15.0 μ mol min⁻¹) under light illumination than that (13.0 μ mol min⁻¹) under dark conditions suggests the plasmon-enhanced HER (Figure S19c). Meanwhile, the unchanged polarization curves after 10 000 cyclic voltammetry sweep cycles (Figure S20) suggest that this catalyst still preserves a superior stability through long-term cycling under light illumination.

In addition, various Au_xNP-in-PdNS electrocatalysts exhibit different HER performances under light illumination, showing a strong dependence on the AuNP size. From Figure 3b,c, Au_{0.50}NP-in-PdNS leads to the largest overpotential decrement (with the average value of 48.3 \pm 0.2 mV) under light illumination compared with the other catalysts (e.g., 38.9 \pm 0.5 and 46.8 \pm 1.8 mV for Au_{0.20}NP-in-PdNS and Au_{1.0}NP-in-

PdNS, respectively). When the content of the Au NP is dramatically increasing (like in Au_{1.0}NP-in-PdNS and Au_{2.0}NPin-PdNS), the degradation in HER performance is observed probably due to the aggregation of Au NPs and rarely intact Pd NS (Figure S4). We hypothesize that the improved apparent catalytic activity of the Au, NP-in-PdNS ($x \le 0.5$) is caused by the LSPR being excited on the Au NPs intercalated in Pd NSs under light illumination. We then studied the electrocatalytic HER of the Au_{0.50}NP-in-PdNS at various wavelengths of light illumination with the same light intensity of 16.8 mW cm⁻². In Figure 3d, the smallest overpotential ($\eta_{10} = 49.7 \pm 1.1 \text{ mV}$) is observed at 520 nm, showing the best catalytic activity. Furthermore, η_{10} decreases at different wavelengths (350, 400, 520, 600, and 700 nm), demonstrating a nonmonotonic curve (the red curve in Figure 3e) that is strongly correlated to the LSPR line shape in the UV-Vis absorption spectrum⁴⁰ of the Au_{0.50}NP-in-PdNS (the green plot in Figure 3e). This correlation lends support to our hypothesis that LSPR effectively enhances the electrocatalytic HER activity of 2D AuNP-in-PdNS heterostructures.

To further demonstrate the plasmon-enhanced electrocatalysis on 2D AuNP-in-PdNS heterostructure, we also study its oxygen reduction reaction (ORR) activity. The ORR performance of AuNP-in-PdNS heterostructure, compared with that of Pt/C (20 wt %), was evaluated in O_2 -

saturated alkaline solution (0.1 M KOH). In Figures S21 and S22, Au_{0.50}NP-in-PdNS exhibits the best ORR performance with both an increased half-wave potential ($E_{1/2}$) of 0.882 V and a limiting current density ($j_{\rm L}$) of 7.5 mA cm⁻² under light illumination compared to those (0.871 V and 6.1 mA) under dark conditions, further verifying plasmonic enhancement in electrocatalytic activity (Table S4). Moreover, the ORR performance of the 2D Au_{0.50}NP-in-PdNS outperforms that of the Pt/C benchmark, resulting in the low overpotential and superior mass transfer for the ORR on this 2D heterostructure.

2.3. Electromagnetic Simulations of the Au, NP-in-PdNS. To elucidate how the LSP effectively enhances the electrocatalytic activity, we performed electromagnetic simulations of the plasmonic effect for the AuxNP-in-PdNS heterostructure using the finite-difference time-domain method (see the Supporting Information for detailed information). $Au_xNP-in-PdNS$ (x =0.05, 0.20, 0.50, 1.0) core-shell structures that match corresponding Au NP sizes (D_{core} = 14, 18, 30, and 46 nm) determined for Au_xNP-in-PdNS catalysts (Figure S4) were simulated to reduce the computation cost without affecting the essence of the plasmonic effect in play. Given that the electronic transitions typically are activated at higher photon energies close to bulk plasmon resonances, here, the quantum-sized effect on the dielectric functions that has been demonstrated in Ag⁴¹ and Au⁴² nanoparticles and thin films^{42,43} was not considered in the simulations. A theoretical model based on Mie theory was employed for calculating absorption spectra and local field distribution. First, we theoretically examined the effect of Au NP size on the LSPR in a series of Au_xNP-in-PdNS core-shell models (Figure 4a, bottom). The LSPR peak shows a redshift, and its line shape becomes more pronounced as the Au NP size becomes larger (Figure 4a, bottom). The simulated absorption spectra well capture the absorption feature in the 500-600 nm wavelength spectral window of the experimental absorption spectra (Figure 4a, top), though the line shapes in the experimental spectra are broader, likely due to the polydispersity of the Au NPs. This agreement confirms that the LSP is being excited on various Au_xNP-in-PdNS catalysts. The feature is further verified by an absorption spectrum of pure Au NPs ($D_{core} = 30 \text{ nm}$) shown in Figure S23 and thus is attributed to optical excitations of Au NP's LSPR. This plasmon-enhanced absorption in the visible range increases the efficiency of harvesting visible light for photoelectrocatalytic reactions. The larger the Au NP size, the stronger the absorption. This trend agrees well with the observation that electrocatalytic activity becomes better as x increases from 0 to 0.5 (Figure 3b). However, as the Au NP size further increases, the electrocatalytic reaction with a certain catalyst loading amount (≥0.102 mg cm⁻²) likely operates in a light-limited regime where all of the photons are either absorbed or scattered, and thus a decrease in electrocatalytic activity is consistent with the higher scattering cross-section (see the blue plot in Figure 4b and Figure S24, and the Supporting Information for detailed information). In addition, the aforementioned conspicuous aggregation of Au NPs and the rarely intact Pd NS, especially in the Au_{1.0}NP-in-PdNS and Au_{2.0}NP-in-PdNS, will somehow hinder the electrocatalytic activity. Thus, all of these factors likely contribute to the opposite size-dependent trend observed in Figure 3b when x >0.5. In other words, an optimal Au NP size (i.e., $D_{core} = 30 \text{ nm}$) and the intact morphology of the 2D Au_{0.50}NP-in-PdNS heterostructure give rise to the highest catalytic activity.

The two-dimensional field enhancement profiles in Figure 4c show that the electromagnetic field of the Au_xNP-in-PdNS core-shell structure is concentrated at the outer surface of the Pd NS shell upon excitation. The local field maximum (hot spot) is very different from that in other core—shell systems (like Au-Ag core-shell),44 where energy is concentrated at both the outer surface of the shell and the core-shell interface. Meanwhile, a larger Au NP results in a higher field enhancement factor with an increase from 12-fold up to 26fold (the red plot in Figure 4b), which is consistent with the size-dependence of plasmon-enhanced absorption observed in Figure 4a at the LSPR wavelengths (~530 nm). However, this correlation might break down when interband transitions are largely involved and thus contribute to absorption heavily. Our calculations show that both field enhancement and the LSPR feature become less pronounced when the Au NP is wrapped by Pd, and they are further weakened when the Pd shell is thicker (Figures S25 and S26). Nevertheless, in our novel 2D heterostructures, the Pd shell (~1.4 nm thickness) minimally wraps the Au NP and thus minimally undermines the plasmonic response while still introducing the indispensable catalytic compartment. When Au_{0.50}NP-in-PdNS core-shell nanostructures aggregate into a dimer, tetramer, or even a chain shown in the inset of Figure 2a, the plasmonic field enhancement further increases by over 2 orders of magnitude and LSPR gains more redshifts (Figures 4d, S27, and S28). Regarding the spacing between Au_{0.50}NP-in-PdNS nanostructures, when it shrinks from 20 nm down to 1 nm, the field enhancement factor increases by 3 orders of magnitude (Figure S29). Although the spacing between Au NPs in our catalysts might vary from one to another, the collective plasmonic effect tremendously contributes to the increased fraction of absorbed photons and stronger field enhancement 45,46 and subsequently enhances electrocatalytic activity.

2.4. Mechanism Discussion. Plasmons can decay via radiative and nonradiative pathways following excitation. 3,47,48 Among nonradiative dissipation pathways, hot charge carriers are generated through interband and/or intraband transitions and then collide with other carriers, forming the hot Fermi-Dirac distribution.³ On the one hand, interband transitions occur in Au at short wavelengths (≤600 nm) through both direct excitations and indirect excitations via Landau damping of plasmons. 49,50 Intraband transitions assisted by phonons or confined surface modes slightly contribute to generating the hot carriers in Au. On the other hand, interband transitions in Pd are favorable over intraband transitions across the entire visible frequency range because of its unfilled d-band intersecting the Fermi level. Thus, interband transitions in both Au and Pd at the LSPR wavelengths are preferential pathways for generating hot carriers. Although the relatively low ratio in the imaginary part of Pd and Au at LSPR wavelengths⁵¹ indicates that plasmon energy more likely dissipates through indirect excitation of interband transitions in Au, the presence of the unique modal features in our Au-Pd heterostructure and the resulting intense field favor charge excitations, which are proportional to the intensity of the local electric field⁵² and hot carriers being concentrated on hotspots of the Pd surface. Eventually, the carrier density on the surface of the Au_xNP-in-PdNS increases due to hot-carrier generation and transfer mediated by the LSP, facilitating the participation of hot carriers in the electrochemical hydrogen evolution process in the wavelength range of LSPR (Figure 3e). Meanwhile, benefiting from the abundant active sites and

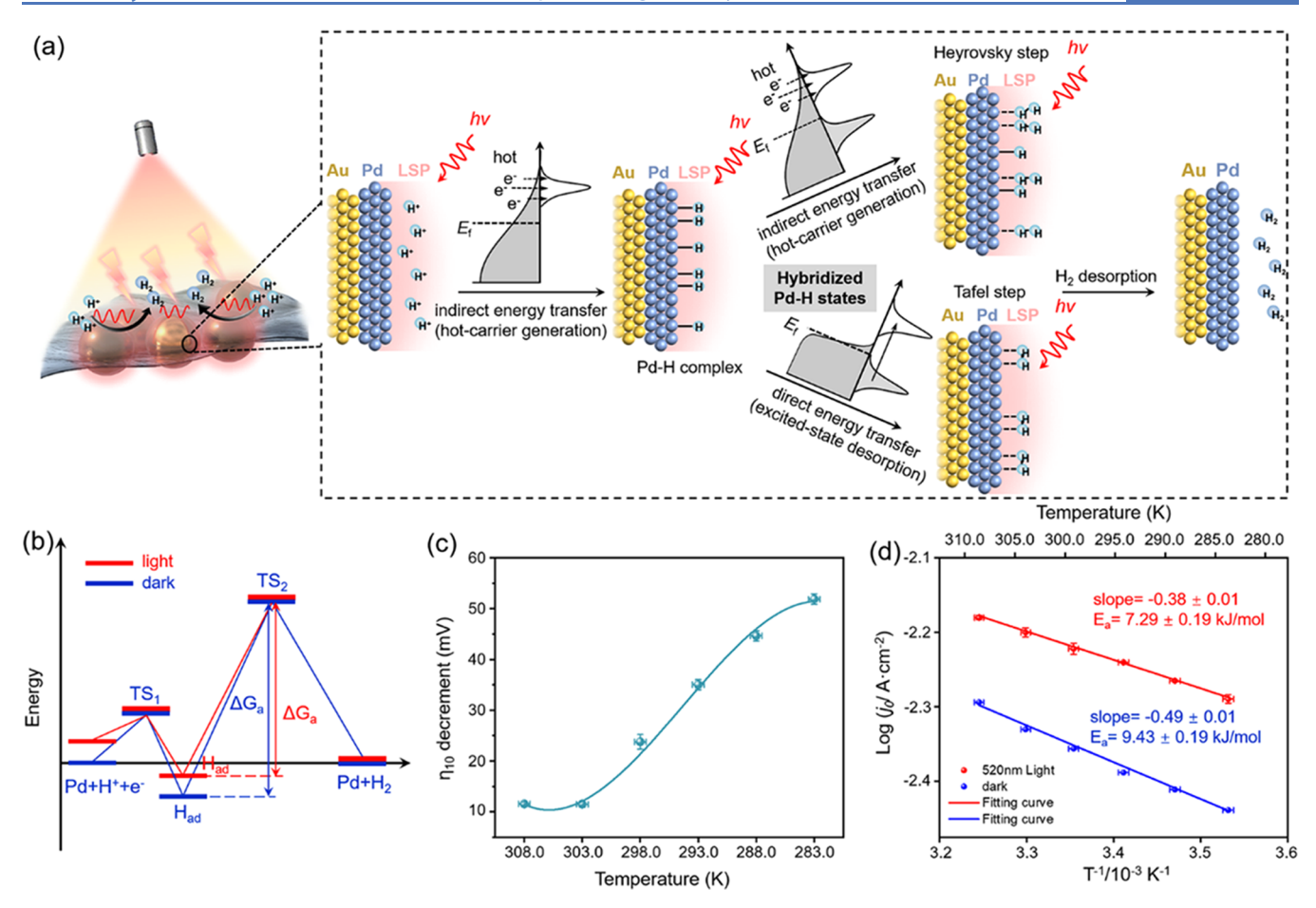


Figure 5. Proposed mechanism for the plasmon-enhanced hydrogen evolution reaction. (a) Schematic of indirect and direct transfer of plasmonic energy for generating hot carriers and promoting excited-state desorption in hydrogen evolution steps, respectively. The hot electrons from the hot Fermi–Dirac distribution transfer to protons forming Pd–H complexes in the Volmer step. The chemisorbed hydrogen atoms desorb from the Pd surface forming H₂ either via the electron transfer resulting from the hot Fermi–Dirac distribution or by exciting Pd–H complexes due to direct transfer of plasmonic energy. (b) Proposed reaction free energy profiles of the HER at equilibrium under dark (blue) and light illumination (red) conditions. (c) Temperature-dependent η_{10} decrement obtained on the Au_{0.50}NP-in-PdNS electrode under light illumination (520 nm, 21.6 mW cm⁻²) and dark conditions. (d) Arrhenius plots of j_0 for the 2D Au_{0.50}NP-in-PdNS heterostructure electrocatalyst over the range of temperature from 283 \pm 0.5 to 308 \pm 0.5 K with an interval of 5 K, from which apparent activation energies are calculated based on their slopes under dark (blue) and 520 nm (21.6 mW cm⁻²) light illumination (red) conditions.

high specific surface area of the ultrathin 2D Pd NSs, these hot carriers can efficiently transport and be exploited for accelerating HER and ORR processes with a much smaller overpotential.

Notwithstanding, direct excitations of interband transitions in both Au and Pd indeed occur and dominate the process of hot-carrier generation at wavelengths close to the ultraviolet region, 53 manifesting as rapidly increasing absorption as the wavelength decreases (Figure 4a). When direct excitations of interband transitions are activated at short wavelengths (<400 nm) beyond LSPR, hot carriers are directly generated in both Au and Pd and then transferred to the catalytic surface for electrochemical conversions. Similar behavior is also observed on the Au nanoparticles for the HER when the electrodes are illuminated at higher photon energies.²⁷ Although these interband transitions contribute to the improved electrocatalytic activity, hot carriers are more vulnerable to a variety of dissipation pathways such as electron-electron, electronphonon scattering, and charge recombination when they migrate through the Au-Pd interface toward the catalytic sites. This behavior is evidenced by a moderately gained but still smaller overpotential decrement at 350 nm for the HER

(Figure 3e). The overpotential decrement might increase again as interband transitions in both Au and Pd via direct excitation contribute more to hot-carrier generation. As indirect and direct excitations taper off at long wavelengths (>650 nm), hot-carrier generation is no longer efficient, thus leading to a very small overpotential decrement at 700 nm. Taken together, the maximum overpotential decrement observed under Xenon light illumination within the wavelength range from 320 to 780 nm mainly results from hot-carrier generation through both indirect excitation of interband transitions in Pd mediated by LSPRs and direct excitation of interband transitions in Au and Pd. In addition to favorable hot-carrier generation in the AuNP-in-PdNS, a direct energy transfer mediated by LSP decay is possible because of the high LSP field intensity and the existence of the electronic states on the Pd surface that might hybridize with states in the chemisorbed hydrogen atoms on the Pd surface. 54,55

Based on the discussion above, we specifically propose a tentative mechanism for plasmon-enhanced HER performance that takes into account both the generation of hot carriers (or indirect energy transfer) and direct energy transfer mediated by LSP decay.³ The LSP exerts a strong impact on both

hydrogen absorption (Volmer step) and desorption (Tafel step) steps in the HER through the involvement of indirect and direct transfer of plasmonic energy. As shown in Figure 5a, the hot carriers, which are readily involved in the proton reduction, are generated on the Pd surface due to both unique modal features of the Au, NP-in-PdNS structure and favorable interband transitions in Pd. The effectively cathodic photocharging⁵⁶ on the 2D Pd NS improves the kinetics of interfacial electron transfer to protons in the electrolyte. The hydrogen atoms chemisorbed on the Pd surface after the Volmer step result in newly hybridized Pd-H states. These states may enable direct momentum-conserved excitations of electrons mediated by the LSP decay like other plasmonic systems featuring adsorbate/metal hybridized states, 57,58 providing a new channel to pass the plasmonic energy directly to the Pd-H complex at the interface and then activating a new reaction path in the desorption process. To clearly elucidate the mechanism of intrinsic plasmon-enhanced HER, we plot reaction free energy profiles under thermodynamic equilibrium (or with zero applied potential) in Figure 5b. Regarding the reaction free energy profiles between dark (Figure 5b, blue) and light illumination (Figure 5b, red) conditions, the initial state under light is much closer to the first transition state (TS₁) due to the hot-electron involvement, making the Volmer step kinetically favorable. The Pd-H complex (H_{ad}) formed in the Volmer step has a lower free energy than that of the initial state because of a negative adsorption free energy of H on the Pd surface under dark conditions.⁵⁹ A direct energy transfer from the LSP to H_{ad} promotes H_{ad} from the ground state to an excited state and, therefore, modifies the desorption reaction pathway. The energy barrier (ΔG_a), i.e., the energy difference between H_{ad} and the second transition state (TS₂), is lowered when H_{ad} is in the excited state (Figure 5b, red). The Tafel slope (<120 mV dec⁻¹) of the Au_{0.50}NP-in-PdNS under light illumination suggests that the desorption step is kinetically limiting.⁶⁰ Thus, the direct energy transfer mechanism may play a vital role in lowering ΔG_a of the intrinsic electrocatalytic HER.

The photothermal effect resulting from hot-carrier thermalization via both electron-phonon scattering in the catalyst and phonon-phonon scattering at the interface between the catalyst and the surrounding medium may affect electrocatalytic reactions by increasing the local temperature. 61 Thus, we explored temperature-dependent behavior by measuring HER polarization curves of the Au_{0.50}NP-in-PdNS at temperatures ranging from 283 to 308 K (Figure S30) under 520 nm light illumination and dark conditions (Figures S31 and S32). η_{10} increases when the temperature decreases from 308 to 283 K under both light illumination and dark conditions (Figure S33), revealing the typical Arrhenius behavior.⁵⁴ Interestingly, the plasmonic enhancement of the HER is much more striking at a lower temperature, evidenced by monotonically increasing η_{10} decrement as temperature drops from 308 to 283 K (with 51.9 mV decrement) (Figure 5c). This behavior likely indicates that the photothermal contribution is minimal in the plasmonenhanced HER because the heat generated through the relaxation of hot electrons leads to a temperature increase of 1.96×10^{-6} K on the surface of the catalyst given the low illumination intensity (21.6 mW cm⁻²) and high thermal conductivity of Pd NS. 61-63 Such a small increase in temperature would not contribute significantly to the large η_{10} decrement at the low temperatures. Based on the polarization curves, the exchange current densities (j_0) and

Tafel slopes were calculated through the Tafel equation ($\eta = a + b \log j$, where a is the intercept obtained through fitting the linear part of the Tafel plot, b is the Tafel slope, η is the overpotential, and j_0 is obtained when $\eta = 0$). In Figure S34, j_0 decreases as the temperature decreases under both dark and 520 nm light illumination conditions. Moreover, using the values of j_0 obtained under both conditions over the temperature range of 283–308 K and Arrhenius equation, we determine the apparent activation energies $(E_a)^{54}$ for the HER (see Section 4 for detailed information). E_a decreases from 9.43 kJ mol⁻¹ under dark to 7.29 kJ mol⁻¹ under light illumination conditions (Figure 5d), further substantiating that the LSP excited on the Au NPs efficiently reduces the energy barrier for the HER.

3. CONCLUSIONS

We present a novel synthetic method in this work that enables plasmonic Au NPs to be intercalated in the ultrathin 2D electrocatalytic Pd NS. This heterostructure with size tunability in Au NPs effectively interfaces LSPRs with the 2D electrocatalyst's abundant active sites and fast chargecarrier transport properties for efficiently enhancing electrocatalytic activity. The decreased overpotential (η_{10}) for electrocatalytic hydrogen evolution and increased half-wave potential and limiting current density for oxygen reduction are achieved on the 2D AuNP-in-PdNS heterostructure under light illumination. The strong correlation between wavelengthdependent electrocatalytic activity and the LSPR line shape implies that the LSPR excitation on Au NPs plays a key role in promoting hydrogen evolution and oxygen reduction performance. Relying on the electromagnetic simulations, we found plasmon-enhanced adsorption and unique plasmonic modal properties in the AuNP-in-PdNS, along with favorable interband transitions in Pd NSs, are of paramount importance to enhance the electrocatalytic performance. These attributes favorably give rise to hot-carrier generation in 2D Pd NSs and mediate the transfer of electron and plasmonic energy for lowering the reaction energy barrier. More importantly, the 2D AuNP-in-PdNS heterostructure will also be promising to act as an electrocatalyst for carbon dioxide reduction or organic electrochemical reactions. This study provides a new avenue for the rational design of efficient plasmon-enhanced electrocatalysts and highlights the distinct role of LSPR excitation in plasmon-enhanced electrocatalysis.

4. EXPERIMENTAL SECTION

4.1. Materials. The chemicals were directly used without further purification— $Pd(acac)_2$ (Alfa Aesar, 99% purity), HAuCl₄ (Alfa Aesar, 99.9% metals basis purity), acetic acid (Innochem, 99.5% purity), acetone (Beijing Chemical Works, \geq 99.5% purity), ethanol (Beijing Chemical Works, 99.7% purity), HClO₄ (Acros, ca. 70% solution in water), Nafion solution (Aldrich, 5 wt-% in lower aliphatic alcohols and water), isopropanol (Beijing Chemical Works, absolute, \geq 99.7% purity), commercial Pt/C (Alfa Aesar, Platinum, 20% on carbon black), and Pd/C (Aldrich, 10% Pd basis). The ultrapure water (18.2 M Ω) purified from Millipore was used in all experiments.

4.2. Synthesis of the Au_xNP-in-PdNS. The 2D Au_xNP-in-PdNS heterostructure was synthesized through a facile wetchemical method combining a three-step process of seed growth, galvanic replacement, and self-assembly (SGA). The

Au_xNP-in-PdNS with various x ratios were synthesized by tuning the mass of HAuCl₄ against Pd(acac)₂, keeping the HAuCl₄/Pd(acac)₂ molar ratios of 0.05, 0.10, 0.15, 0.20, 0.50, 1.0, and 2.0, in 10 mL of acetic acid. For instance, when synthesizing the Au_{0.05}NP-in-PdNS, 15.2 mg of Pd(acac)₂ and 125 μ L of 20 mM HAuCl₄ solution were simultaneously dissolved in 10 mL of acetic acid; then, CO gas bubbled the solution at a speed of 200 mL min⁻¹ for 30 min, followed by incubation under sealed conditions for 24 h. The obtained precipitant was collected after high-speed centrifugation and thoroughly washed with acetone and ethanol. Finally, the various Au_xNP-in-PdNS samples were dispersed in the ethanol solvent with a concentration of 1 mg mL⁻¹ for further usage.

- **4.3. Synthesis of Pd NSs.** The Pd NS catalyst was prepared according to the previous report³⁷ with minor modifications. Typically, Pd(acac)₂ (15.2 mg, 5 mmol) was dissolved in 10 mL of acetic acid to form a homogeneous solution. Subsequently, CO gas was introduced by bubbling at a speed of 200 mL min⁻¹ for 30 min, followed by incubation under sealed conditions for 24 h. The obtained precipitant was separated by centrifugation and thoroughly washed with acetone and ethanol. The Pd NSs were dispersed in ethanol with a concentration of 1 mg mL⁻¹.
- **4.4.** Material Characterization. The morphologies of Au, NP-in-PdNS were characterized using a transmission electron microscope (TEM, FEI Tecnai G2 F20), an aberration-corrected high-resolution transmission electron microscope (JEM ARM200F) at 200 kV equipped with energy-dispersive X-ray (EDX) analysis, and a scanning electron microscope (SEM, Hitachi S-4800). The powder Xray diffraction (XRD, Bruker D8 Focus) was used to determine the crystal structure of the 2D Au_xNP-in-PdNS. Inductively coupled plasma optical emission spectroscopy (ICP-OES) analysis was carried out on a Thermo Scientific iCAP 6300 to confirm the exact composition of various Au/Pd ratios of the 2D Au_xNP-in-PdNS heterostructure. X-ray photoelectron spectroscopy (XPS) analysis was performed on a Thermo Fisher ESCALAB 250Xi to further study the composition of various Au_xNP-in-PdNS. UV-Vis absorption spectra were collected from a Multimode Plate Reader (PerkinElmer EnSpire).
- **4.5. Electrode Preparation.** For working electrode preparation, drop-casted catalyst powders were prepared on a rotating disk electrode (RDE, Pine Research Instrumentation) made of a glass carbon disk (with a geometric area of 0.196 cm²). Prior to electrode preparation, the RDE was polished with 1, 0.3, and 0.05 μ m alumina suspensions on a polishing cloth successively, thoroughly rinsed with Milli-Q water and ethanol, briefly sonicated in ethanol for less than 30 s, and dried under ambient conditions. Au, NP-in-PdNS and Pd NS catalyst inks were prepared by suspending 500 μL of 1.0 mg mL⁻¹ preprepared solution and 20 μL of 5 wt % Nafion solution in 1.48 mL of isopropanol via sonication for 0.5 h. Then, 80 μ L of catalyst ink was drop-casted onto the RDE and dried under ambient conditions to form a uniform catalyst film with a fixed catalyst loading of 0.102 mg cm⁻². As a comparison, the Pd/C and Pt/C catalyst inks were prepared by suspending 500 μ L of 1.0 mg mL⁻¹ prepared solution, in which 0.5 mg of 20 wt % Pd/C and Pt/C commercial powder were predispersed in 0.5 mL of ethanol, and 20 μ L of 5 wt % Nafion solution in 1.48 mL of isopropanol via sonication for 0.5 h. To prepare Pd/C and Pt/C electrodes, 80 μ L of ink was then drop-casted onto the RDE and dried under ambient

conditions to form a uniform catalyst film with the same catalyst loading of 0.102 mg cm $^{-2}$. The carbon paper electrode with the Au_{0.50}NP-in-PdNS catalyst was prepared and tested to determine the H₂ evolution. For the corresponding electrode preparation, the Au_{0.50}NP-in-PdNS catalyst ink was drop-casted on the carbon paper, which is successively cleaned in the ethanol, acetone, DI water, and then dried.

4.6. Plasmon-Enhanced Electrocatalysis Measurements. 4.6.1. Plasmon-Enhanced Hydrogen Evolution Reaction (HER) Measurements. All electrochemical measurements were conducted in an undivided three-electrode cell connected to an electrochemical workstation (Princeton Applied Research Parstat. MC). For the convenience of light illumination, a quartz cell was utilized during the measurement. A graphite rod and a saturated calomel electrode (SCE, saturated KCl) were used as the counter and reference electrodes, respectively. HClO₄ (1.0 M, pH ≈ 0.09) was utilized as an acidic electrolyte. Prior to each measurement, the electrolyte solution was purged and saturated with N2 gas. A home-made cell system (Figure S12) was applied to achieve the photoenhanced hydrogen evolution reaction (HER) measurements with the help of a 300 W Xenon lamp. Various monochromatic light was controlled with a cut-off filter of different wavelengths ($\lambda = 350, 400, 520, 600, \text{ and } 700 \text{ nm}$) at a fixed light intensity of 16.8 mW cm⁻². All experiments were performed isothermally, i.e., keeping the temperature of the reference electrode and the working electrode same and varied from 308 to 283 K at 5 K intervals. At the same time, the temperatures in the bulk electrolyte and the area around 5 mm away from the electrode surface were measured using a digital thermometer (Anymetre PT3001). The measured temperatures are presented in Table S5. During the measurement, a home-made three-electrode cell equipped with a water bath was utilized and the temperature of the electrolyte was accordingly measured with a thermometer (Figure S12a). Finally, all potentials were corrected to the reversible hydrogen electrode (RHE) scale after iR-correction at the same temperature according to the Nernst equation (eq 1)

$$V_{\text{vs RHE}} = V_{\text{vs SCE}} + E_{\text{SCE},T}^{\theta} + \frac{2.3025RT}{F} \times \text{pH}$$
 (1)

where *R* is the universal gas constant ($R = 8.314 \text{ K}^{-1} \text{ mol}^{-1}$), *T* (K) is the temperature, F is the Faraday constant (96 485.3 J mol^{-1}), and $E_{\text{SCE,T}}^{\theta}$ is the standard electrode potentials at different temperatures. Linear scan voltammetry (LSV) at 5 mV s⁻¹ was performed on different electrodes, which were vigorously rotated at 1600 rpm. For stability evaluation of the Au_{0.50}NP-in-PdNS electrode, the continuous chronopotentiometry test at 10 mA cm⁻² and 10 000 cyclic voltammetry sweep cycles were conducted under dark and Xenon light illumination. The series resistance (R_s) and charge-transfer resistance (R_{ct}) over the different conditions were obtained by electrochemical impedance spectroscopy (EIS, Figure S15). Based on the exchange current densities (j_0) at different temperatures, the apparent activation energies for the hydrogen evolution on the Au_{0.50}NP-in-PdNS electrode under dark and 520 nm light illumination conditions (21.6 mW cm⁻²) were determined according to the Arrhenius equation

$$d(\log j_0) = -\frac{E_a}{2.3R}d(1/T)$$
(2)

where E_a is the apparent activation energy for hydrogen evolution on the catalyst and j_0 is the exchange current density.

For testing the produced H_2 in the plasmon-enhanced HER measurement, a sealed H-type electrolyzer (Figure S19a) was utilized. The prepared carbon paper electrode acted as the working electrode. The produced H_2 gas was analyzed using an online gas chromatograph (Shimadzu GC-2014) equipped with a thermal conductivity detector, a Molsieve 5 Å column, and a flame ionization detector.

4.6.2. Plasmon-Enhanced Oxygen Reduction Reaction (ORR) Measurements. The electrochemical ORR properties were evaluated in a three-electrode cell that was composed of a glassy-carbon rotating disk electrode (RDE) with an area of 0.196 cm² as the working electrode, along with the Hg/HgO reference electrode (1 M KOH) and a platinum wire counter electrode in a 0.1 M KOH electrolyte. Prior to each measurement, the electrolyte solution was purged with oxygen for 30 min to saturate and then bubble it continuously. The measurements were conducted at a scan rate of 10 mV s⁻¹ and a rotation rate of 1600 rpm, respectively. The photoenhanced oxygen reduction reaction (ORR) was measured at ~25 °C under a 300 W Xenon lamp. During the measurement, the same home-made three-electrode cell equipped with a water bath was utilized and the temperature of the electrolyte was accordingly measured with a thermometer (Figure S12a). Finally, all potentials were corrected to the reversible hydrogen electrode (RHE) scale by iR-correction according to the Nernst equation (eq 3)

$$V_{\text{vs RHE}} = V_{\text{vs Hg/HgO}} + E_{\text{Hg/HgO},T}^{\theta} + 0.059 \times \text{pH}$$
(3)

where $E_{\rm Hg/HgO,\,T}^{\theta}$ is the standard electrode potential. Here, T is 25 °C.

4.7. Electromagnetic Simulations. The optical properties of the AuxNP-in-PdNS heterostructure were simulated using the finite-difference time-domain (FDTD) method. All of the models were established and implemented in the package of FDTD solutions (Lumerical, Inc.). The Au NP was modeled as a sphere with different diameters (14, 18, 30, or 46 nm) and with the refractive index taken from the material database of CRC.64 The Pd NS that wraps the Au NP was modeled as an etched sphere surrounding the Au NP-sphere with different thicknesses (1.5, 6, or 12 nm) and with the refractive index taken from the material database of Palik.⁶⁵ Total-field/scattered-field light source conditions were employed throughout all of the simulations. The incident field injected along the z-axis was polarized along the x-axis, and the wavelength range was set from 300 to 800 nm. Water was chosen as the background medium with a refractive index of 1.33. The nonuniform mesh was used in the simulation region. A mesh sweeping converging test was run to choose proper mesh sizes for individual components in the simulation region. The absorption and scattering spectra (not shown) were calculated based on the Mie theory within the formalism of the total-field/scattered-field. The fraction of absorption was calculated as a ratio of the total photon energy being absorbed to the sum of the total energy being absorbed and scattered by the electrocatalysts under broadband illumination of the Xenon lamp. The electromagnetic field distributions in the x-y plane were obtained at each wavelength via the standard Fourier transform, and only the field enhancement profiles at the LSPR wavelength are shown in the main text and the Supporting Information.

ASSOCIATED CONTENT

Supporting Information

The Supporting Information is available free of charge at https://pubs.acs.org/doi/10.1021/acscatal.1c03811.

TEM, HRTEM, and SEM images of Pd NSs and Au_xNP-in-PdNS; particle size distribution, ex situ TEM, and UV-Vis absorption spectra characterization of the intermediates during the synthesis; EDX mapping; XRD patterns; XPS spectra of various Au_xNP-in-PdNS LSV curves, EIS, Tafel plots, CV curves, and ECSA determination of Au_xNP-in-PdNS for the HER; determination of produced H₂ gas, plasmon-enhanced ORR electrocatalysis, simulated absorption spectra, two-dimensional field enhancement profiles, exchange current densities obtained under different temperatures; and comparison of the performance with other structured Pd-based electrocatalysts for the HER and the ORR (PDF)

AUTHOR INFORMATION

Corresponding Authors

Shuangfei Cai — CAS Key Laboratory for Biomedical Effects of Nanomaterials and Nanosafety, CAS Key Laboratory of Nanosystem and Hierarchical Fabrication, Center of Materials Science and Optoelectronics Engineering, CAS Center for Excellence in Nanoscience, National Center for Nanoscience and Technology, University of Chinese Academy of Sciences, Beijing 100190, P. R. China; orcid.org/0000-0002-8122-684X; Email: caisf@nanoctr.cn

Rong Yang — CAS Key Laboratory for Biomedical Effects of Nanomaterials and Nanosafety, CAS Key Laboratory of Nanosystem and Hierarchical Fabrication, Center of Materials Science and Optoelectronics Engineering, CAS Center for Excellence in Nanoscience, National Center for Nanoscience and Technology, University of Chinese Academy of Sciences, Beijing 100190, P. R. China; orcid.org/0000-0002-6112-3149; Email: yangr@nanoctr.cn

Jun He — Key Laboratory of Artificial Micro- and Nanostructures of Ministry of Education, School of Physics and Technology, Wuhan University, Wuhan 430072, P. R. China; orcid.org/0000-0002-2355-7579; Email: hej@nanoctr.cn

Authors

Jianwei Ding — CAS Key Laboratory for Biomedical Effects of Nanomaterials and Nanosafety, CAS Key Laboratory of Nanosystem and Hierarchical Fabrication, Center of Materials Science and Optoelectronics Engineering, CAS Center for Excellence in Nanoscience, National Center for Nanoscience and Technology, University of Chinese Academy of Sciences, Beijing 100190, P. R. China

Fengmei Wang — CAS Key Laboratory for Biomedical Effects of Nanomaterials and Nanosafety, CAS Key Laboratory of Nanosystem and Hierarchical Fabrication, Center of Materials Science and Optoelectronics Engineering, CAS Center for Excellence in Nanoscience, National Center for Nanoscience and Technology, University of Chinese Academy of Sciences, Beijing 100190, P. R. China; orcid.org/0000-0002-9438-9859

Feng Pan – Department of Chemistry, University of Wisconsin-Madison, Madison, Wisconsin 53706, United States; Occid.org/0000-0002-0262-5843

- Peng Yu CAS Key Laboratory for Biomedical Effects of Nanomaterials and Nanosafety, CAS Key Laboratory of Nanosystem and Hierarchical Fabrication, Center of Materials Science and Optoelectronics Engineering, CAS Center for Excellence in Nanoscience, National Center for Nanoscience and Technology, University of Chinese Academy of Sciences, Beijing 100190, P. R. China
- Ning Gao CAS Key Laboratory for Biomedical Effects of Nanomaterials and Nanosafety, CAS Key Laboratory of Nanosystem and Hierarchical Fabrication, Center of Materials Science and Optoelectronics Engineering, CAS Center for Excellence in Nanoscience, National Center for Nanoscience and Technology, University of Chinese Academy of Sciences, Beijing 100190, P. R. China

Randall H. Goldsmith – Department of Chemistry, University of Wisconsin-Madison, Madison, Wisconsin 53706, United States; © orcid.org/0000-0001-9083-8592

Complete contact information is available at: https://pubs.acs.org/10.1021/acscatal.1c03811

Author Contributions

J.D., F.W., and F.P. contributed equally.

Notes

The authors declare no competing financial interest.

ACKNOWLEDGMENTS

This work is supported by the Strategic Priority Research Program of the Chinese Academy of Sciences (XDB36000000), the National Key R&D Program of China (Nos. 2021YFE0112600 and 2018YFA0703700), the National Natural Science Foundation of China (Nos. 21805057 and 61625401), and the National Science Foundation (USA, CHE-1856518). F.W., P.Y., and N.G. acknowledge the support from the CAS Key Laboratory of Nanosystem and Hierarchical Fabrication.

REFERENCES

- (1) Zhang, Y.; He, S.; Guo, W.; Hu, Y.; Huang, J.; Mulcahy, J. R.; Wei, W. D. Surface-Plasmon-Driven Hot Electron Photochemistry. *Chem. Rev.* **2018**, *118*, 2927–2954.
- (2) Corson, E. R.; Creel, E. B.; Kostecki, R.; McCloskey, B. D.; Urban, J. J. Important Considerations in Plasmon-Enhanced Electrochemical Conversion at Voltage-Biased Electrodes. *iScience* **2020**, 23, No. 100911
- (3) Aslam, U.; Rao, V. G.; Chavez, S.; Linic, S. Catalytic Conversion of Solar to Chemical Energy on Plasmonic Metal Nanostructures. *Nat. Catal.* **2018**, *1*, 656–665.
- (4) Sytwu, K.; Vadai, M.; Dionne, J. A. Bimetallic Nanostructures: Combining Plasmonic and Catalytic Metals for Photocatalysis. *Adv. Phys.: X* **2019**, *4*, No. 1619480.
- (5) Sytwu, K.; Vadai, M.; Hayee, F.; Angell, D. K.; Dai, A.; Dixon, J.; Dionne, J. A. Driving Energetically Unfavorable Dehydrogenation Dynamics with Plasmonics. *Science* **2021**, *371*, 280–283.
- (6) Vadai, M.; Angell, D. K.; Hayee, F.; Sytwu, K.; Dionne, J. A. In-Situ Observation of Plasmon-Controlled Photocatalytic Dehydrogenation of Individual Palladium Nanoparticles. *Nat. Commun.* **2018**, *9*, No. 4658.
- (7) Wang, C.; Yang, W.-C. D.; Raciti, D.; Bruma, A.; Marx, R.; Agrawal, A.; Sharma, R. Endothermic Reaction at Room Temperature Enabled by Deep-Ultraviolet Plasmons. *Nat. Mater.* **2021**, *20*, 346–352.
- (8) Li, K.; Hogan, N. J.; Kale, M. J.; Halas, N. J.; Nordlander, P.; Christopher, P. Balancing Near-Field Enhancement, Absorption, and Scattering for Effective Antenna—Reactor Plasmonic Photocatalysis. *Nano Lett.* **2017**, *17*, 3710—3717.

- (9) Swearer, D. F.; Zhao, H.; Zhou, L.; Zhang, C.; Robatjazi, H.; Martirez, J. M.; Krauter, C. M.; Yazdi, S.; McClain, M. J.; Ringe, E.; Carter, E. A.; Nordlander, P.; Halas, N. J. Heterometallic Antenna-Reactor Complexes for Photocatalysis. *Proc. Natl. Acad. Sci. U.S.A.* **2016**, *113*, 8916–8920.
- (10) Robatjazi, H.; Zhao, H.; Swearer, D. F.; Hogan, N. J.; Zhou, L.; Alabastri, A.; McClain, M. J.; Nordlander, P.; Halas, N. J. Plasmon-Induced Selective Carbon Dioxide Conversion on Earth-Abundant Aluminum-Cuprous Oxide Antenna-Reactor Nanoparticles. *Nat. Commun.* **2017**, *8*, No. 27.
- (11) Engelbrekt, C.; Crampton, K. T.; Fishman, D. A.; Law, M.; Apkarian, V. A. Efficient Plasmon-Mediated Energy Funneling to the Surface of Au@Pt Core—Shell Nanocrystals. *ACS Nano* **2020**, *14*, 5061–5074.
- (12) Xu, P.; Lu, W.; Zhang, J.; Zhang, L. Efficient Hydrolysis of Ammonia Borane for Hydrogen Evolution Catalyzed by Plasmonic Ag@Pd Core—Shell Nanocubes. *ACS Sustainable Chem. Eng.* **2020**, 8, 12366–12377.
- (13) Huang, H.; Zhang, L.; Lv, Z.; Long, R.; Zhang, C.; Lin, Y.; Wei, K.; Wang, C.; Chen, L.; Li, Z. Y.; Zhang, Q.; Luo, Y.; Xiong, Y. Unraveling Surface Plasmon Decay in Core-Shell Nanostructures toward Broadband Light-Driven Catalytic Organic Synthesis. *J. Am. Chem. Soc.* **2016**, *138*, 6822–6828.
- (14) Aslam, U.; Chavez, S.; Linic, S. Controlling Energy Flow in Multimetallic Nanostructures for Plasmonic Catalysis. *Nat. Nanotechnol.* **2017**, *12*, 1000–1005.
- (15) Sarina, S.; Zhu, H.; Jaatinen, E.; Xiao, Q.; Liu, H.; Jia, J.; Chen, C.; Zhao, J. Enhancing Catalytic Performance of Palladium in Gold and Palladium Alloy Nanoparticles for Organic Synthesis Reactions through Visible Light Irradiation at Ambient Temperatures. *J. Am. Chem. Soc.* **2013**, *135*, 5793–5801.
- (16) Lin, S.-C.; Hsu, C.-S.; Chiu, S.-Y.; Liao, T.-Y.; Chen, H. M. Edgeless Ag—Pt Bimetallic Nanocages: In Situ Monitor Plasmon-Induced Suppression of Hydrogen Peroxide Formation. *J. Am. Chem. Soc.* **2017**, *139*, 2224—2233.
- (17) Zheng, Z.; Tachikawa, T.; Majima, T. Plasmon-Enhanced Formic Acid Dehydrogenation Using Anisotropic Pd–Au Nanorods Studied at the Single-Particle Level. *J. Am. Chem. Soc.* **2015**, *137*, 948–957
- (18) Christopher, P.; Xin, H.; Marimuthu, A.; Linic, S. Singular Characteristics and Unique Chemical Bond Activation Mechanisms of Photocatalytic Reactions on Plasmonic Nanostructures. *Nat. Mater.* **2012**, *11*, 1044–1050.
- (19) Robatjazi, H.; Bahauddin, S. M.; Doiron, C.; Thomann, I. Direct Plasmon-Driven Photoelectrocatalysis. *Nano Lett.* **2015**, *15*, 6155–6161.
- (20) Gargiulo, J.; Berté, R.; Li, Y.; Maier, S. A.; Cortés, E. From Optical to Chemical Hot Spots in Plasmonics. *Acc. Chem. Res.* **2019**, 52, 2525–2535.
- (21) Cortés, E.; Xie, W.; Cambiasso, J.; Jermyn, A. S.; Sundararaman, R.; Narang, P.; Schlücker, S.; Maier, S. A. Plasmonic Hot Electron Transport Drives Nano-Localized Chemistry. *Nat. Commun.* **2017**, *8*, No. 14880.
- (22) Zhou, L.; Swearer, D. F.; Zhang, C.; Robatjazi, H.; Zhao, H.; Henderson, L.; Dong, L.; Christopher, P.; Carter, E. A.; Nordlander, P.; Halas, N. J. Quantifying Hot Carrier and Thermal Contributions in Plasmonic Photocatalysis. *Science* **2018**, *362*, 69–72.
- (23) Creel, E. B.; Corson, E. R.; Eichhorn, J.; Kostecki, R.; Urban, J. J.; McCloskey, B. D. Directing Selectivity of Electrochemical Carbon Dioxide Reduction Using Plasmonics. *ACS Energy Lett.* **2019**, *4*, 1098–1105.
- (24) Shi, F.; He, J.; Zhang, B.; Peng, J.; Ma, Y.; Chen, W.; Li, F.; Qin, Y.; Liu, Y.; Shang, W.; Tao, P.; Song, C.; Deng, T.; Qian, X.; Ye, J.; Wu, J. Plasmonic-Enhanced Oxygen Reduction Reaction of Silver/Graphene Electrocatalysts. *Nano Lett.* **2019**, *19*, 1371–1378.
- (25) Zheng, Z.; Xie, W.; Li, M.; Ng, Y. H.; Wang, D.-W.; Dai, Y.; Huang, B.; Amal, R. Platinum Electrocatalysts with Plasmonic Nano-Cores for Photo-Enhanced Oxygen-Reduction. *Nano Energy* **2017**, *41*, 233–242.

- (26) Guo, X.; Li, X.; Kou, S.; Yang, X.; Hu, X.; Ling, D.; Yang, J. Plasmon-Enhanced Electrocatalytic Hydrogen/Oxygen Evolution by Pt/Fe—Au Nanorods. *J. Mater. Chem. A* **2018**, *6*, 7364—7369.
- (27) Wilson, A. J.; Mohan, V.; Jain, P. K. Mechanistic Understanding of Plasmon-Enhanced Electrochemistry. *J. Phys. Chem. C* **2019**, *123*, 29360–29369.
- (28) Hammer, B.; Norskov, J. K. Why Gold is the Noblest of All the Metals. *Nature* **1995**, *376*, 238–240.
- (29) Shang, B.; Cui, X.; Jiao, L.; Qi, K.; Wang, Y.; Fan, J.; Yue, Y.; Wang, H.; Bao, Q.; Fan, X.; Wei, S.; Song, W.; Cheng, Z.; Guo, S.; Zheng, W. Lattice-Mismatch-Induced Ultrastable 1T-Phase MoS₂-Pd/Au for Plasmon-Enhanced Hydrogen Evolution. *Nano Lett.* **2019**, 19, 2758–2764.
- (30) Shi, Y.; Wang, J.; Wang, C.; Zhai, T. T.; Bao, W. J.; Xu, J. J.; Xia, X. H.; Chen, H. Y. Hot Electron of Au Nanorods Activates the Electrocatalysis of Hydrogen Evolution on MoS₂ Nanosheets. *J. Am. Chem. Soc.* **2015**, *137*, 7365–7370.
- (31) Wang, S. S.; Jiao, L.; Qian, Y.; Hu, W. C.; Xu, G. Y.; Wang, C.; Jiang, H. L. Boosting Electrocatalytic Hydrogen Evolution over Metal-Organic Frameworks by Plasmon-Induced Hot-Electron Injection. *Angew. Chem., Int. Ed.* **2019**, *58*, 10713–10717.
- (32) Zhang, Z.; Liu, Y.; Chen, B.; Gong, Y.; Gu, L.; Fan, Z.; Yang, N.; Lai, Z.; Chen, Y.; Wang, J.; Huang, Y.; Sindoro, M.; Niu, W.; Li, B.; Zong, Y.; Yang, Y.; Huang, X.; Huo, F.; Huang, W.; Zhang, H. Submonolayered Ru Deposited on Ultrathin Pd Nanosheets Used for Enhanced Catalytic Applications. *Adv. Mater.* **2016**, *28*, 10282–10286.
- (33) Ge, J.; He, D.; Chen, W.; Ju, H.; Zhang, H.; Chao, T.; Wang, X.; You, R.; Lin, Y.; Wang, Y.; Zhu, J.; Li, H.; Xiao, B.; Huang, W.; Wu, Y.; Hong, X.; Li, Y. Atomically Dispersed Ru on Ultrathin Pd Nanoribbons. *I. Am. Chem. Soc.* **2016**, *138*, 13850–13853.
- (34) Fan, Z.; Huang, X.; Han, Y.; Bosman, M.; Wang, Q.; Zhu, Y.; Liu, Q.; Li, B.; Zeng, Z.; Wu, J.; Shi, W.; Li, S.; Gan, C. L.; Zhang, H. Surface Modification-Induced Phase Transformation of Hexagonal Close-Packed Gold Square Sheets. *Nat. Commun.* **2015**, *6*, No. 6571.
- (35) Bratsch, S. G. Standard Electrode Potentials and Temperature Coefficients in Water at 298.15 K. J. Phys. Chem. Ref. Data 1989, 18, 1–21.
- (36) Yin, X.; Warren, S. A.; Pan, Y.-T.; Tsao, K.-C.; Gray, D. L.; Bertke, J.; Yang, H. A Motif for Infinite Metal Atom Wires. *Angew. Chem., Int. Ed.* **2014**, *53*, 14087–14091.
- (37) Yin, X.; Liu, X.; Pan, Y.-T.; Walsh, K. A.; Yang, H. Hanoi Tower-like Multilayered Ultrathin Palladium Nanosheets. *Nano Lett.* **2014**, *14*, 7188–7194.
- (38) Huang, X.; Tang, S.; Mu, X.; Dai, Y.; Chen, G.; Zhou, Z.; Ruan, F.; Yang, Z.; Zheng, N. Freestanding Palladium Nanosheets with Plasmonic and Catalytic Properties. *Nat. Nanotechnol.* **2011**, *6*, 28–32
- (39) Chen, A.; Ostrom, C. Palladium-Based Nanomaterials: Synthesis and Electrochemical Applications. *Chem. Rev.* **2015**, *115*, 11999–12044.
- (40) Yu, Y.; Wijesekara, K. D.; Xi, X.; Willets, K. A. Quantifying Wavelength-Dependent Plasmonic Hot Carrier Energy Distributions at Metal/Semiconductor Interfaces. *ACS Nano* **2019**, *13*, 3629–3637.
- (41) Scholl, J. A.; Koh, A. L.; Dionne, J. A. Quantum Plasmon Resonances of Individual Metallic Nanoparticles. *Nature* **2012**, *483*, 421–427.
- (42) Liu, G. Electron Surface Scattering and Quantum Finite-Size Effect on Dielectric and Optical Properties of Thin Gold Films. *Superlattices Microstruct.* **2019**, 125, 322–329.
- (43) Zhang, G.; Yu, M.; Tung, C.; Lo, G. Quantum Size Effects on Dielectric Constants and Optical Absorption of Ultrathin Silicon Films. *IEEE Electron Device Lett.* **2008**, *29*, 1302–1305.
- (44) Zhang, C.; Chen, B.-Q.; Li, Z.-Y.; Xia, Y.; Chen, Y.-G. Surface Plasmon Resonance in Bimetallic Core—Shell Nanoparticles. *J. Phys. Chem. C* 2015, 119, 16836—16845.
- (45) Yu, G.; Qian, J.; Zhang, P.; Zhang, B.; Zhang, W.; Yan, W.; Liu, G. Collective Excitation of Plasmon-Coupled Au-Nanochain Boosts

- Photocatalytic Hydrogen Evolution of Semiconductor. *Nat. Commun.* **2019**, *10*, No. 4912.
- (46) Halas, N. J.; Lal, S.; Chang, W.-S.; Link, S.; Nordlander, P. Plasmons in Strongly Coupled Metallic Nanostructures. *Chem. Rev.* **2011**, *111*, 3913–3961.
- (47) Sönnichsen, C.; Franzl, T.; Wilk, T.; von Plessen, G.; Feldmann, J.; Wilson, O.; Mulvaney, P. Drastic Reduction of Plasmon Damping in Gold Nanorods. *Phys. Rev. Lett.* **2002**, *88*, No. 077402.
- (48) Pan, F.; Smith, K. C.; Nguyen, H. L.; Knapper, K. A.; Masiello, D. J.; Goldsmith, R. H. Elucidating Energy Pathways through Simultaneous Measurement of Absorption and Transmission in a Coupled Plasmonic-Photonic Cavity. *Nano Lett.* **2020**, *20*, 50–58.
- (49) Sundararaman, R.; Narang, P.; Jermyn, A. S.; Goddard, W. A., III; Atwater, H. A. Theoretical Predictions for Hot-Carrier Generation from Surface Plasmon Decay. *Nat. Commun.* **2014**, *5*, No. 5788.
- (50) Kim, Y.; Smith, J. G.; Jain, P. K. Harvesting Multiple Electron—Hole Pairs Generated through Plasmonic Excitation of Au Nanoparticles. *Nat. Chem.* **2018**, *10*, 763–769.
- (51) Chavez, S.; Aslam, U.; Linic, S. Design Principles for Directing Energy and Energetic Charge Flow in Multicomponent Plasmonic Nanostructures. *ACS Energy Lett.* **2018**, *3*, 1590–1596.
- (52) Christopher, P.; Moskovits, M. Hot Charge Carrier Transmission from Plasmonic Nanostructures. *Annu. Rev. Phys. Chem.* **2017**, *68*, 379–398.
- (53) Sarina, S.; Zhu, H. Y.; Xiao, Q.; Jaatinen, E.; Jia, J.; Huang, Y.; Zheng, Z.; Wu, H. Viable Photocatalysts under Solar-Spectrum Irradiation: Nonplasmonic Metal Nanoparticles. *Angew. Chem., Int. Ed.* **2014**, *53*, 2935–2940.
- (54) Marković, N. M.; Grgur, B. N.; Ross, P. N. Temperature-Dependent Hydrogen Electrochemistry on Platinum Low-Index Single-Crystal Surfaces in Acid Solutions. *J. Phys. Chem. B* **1997**, *101*, 5405–5413.
- (55) Vadai, M.; Angell, D. K.; Hayee, F.; Sytwu, K.; Dionne, J. A. In-Situ Observation of Plasmon-Controlled Photocatalytic Dehydrogenation of Individual Palladium Nanoparticles. *Nat. Commun.* **2018**, *9*, No. 4658.
- (56) Kim, Y.; Torres, D.; Jain, P. K. Activation Energies of Plasmonic Catalysts. *Nano Lett.* **2016**, *16*, 3399–3407.
- (57) Boerigter, C.; Campana, R.; Morabito, M.; Linic, S. Evidence and Implications of Direct Charge Excitation as the Dominant Mechanism in Plasmon-Mediated Photocatalysis. *Nat. Commun.* **2016**, *7*, No. 10545.
- (58) Yan, J.; Jacobsen, K. W.; Thygesen, K. S. First-Principles Study of Surface Plasmons on Ag(111) and H/Ag(111). *Phys. Rev. B* **2011**, 84, No. 235430.
- (59) Jaramillo, T. F.; Jørgensen, K. P.; Bonde, J.; Nielsen, J. H.; Horch, S.; Chorkendorff, I. Identification of Active Edge Sites for Electrochemical H₂ Evolution from MoS₂ Nanocatalysts. *Science* **2007**, *317*, 100–102.
- (60) Conway, B. E.; Tilak, B. V. Interfacial Processes Involving Electrocatalytic Evolution and Oxidation of H₂, and the Role of Chemisorbed H. *Electrochim. Acta* **2002**, *47*, 3571–3594.
- (61) Wang, F.; Li, C.; Chen, H.; Jiang, R.; Sun, L.-D.; Li, Q.; Wang, J.; Yu, J. C.; Yan, C.-H. Plasmonic Harvesting of Light Energy for Suzuki Coupling Reactions. J. Am. Chem. Soc. 2013, 135, 5588–5601.
- (62) Huschka, R.; Zuloaga, J.; Knight, M. W.; Brown, L. V.; Nordlander, P.; Halas, N. J. Light-Induced Release of DNA from Gold Nanoparticles: Nanoshells and Nanorods. *J. Am. Chem. Soc.* **2011**, 133, 12247–12255.
- (63) Baffou, G.; Quidant, R.; García de Abajo, F. J. Nanoscale Control of Optical Heating in Complex Plasmonic Systems. *ACS Nano* **2010**, *4*, 709–716.
- (64) Haynes, W. M. CRC Handbook of Chemistry and Physics, 95th ed.; CRC Press: Boulder, 2014.
- (65) Palik, E. Handbook of Optical Constants of Solids: Index; Academic Press, 1988; Vol. 3.